

The Kinematics of Polycyclic Aromatic Hydrocarbons (PAHs) in Galaxies revealed by Principal Component Analysis (PCA) tomography with JWST/NIRSpec.

Fergus R. Donnan, ¹* Dimitra Rigopoulou,^{1,2} Ismael García-Bernete ¹

¹*Department of Physics, University of Oxford, Keble Road, Oxford, OX1 3RH, UK*

²*School of Sciences, European University Cyprus, Diogenes street, Engomi, 1516 Nicosia, Cyprus*

Accepted XXX. Received YYY; in original form ZZZ

ABSTRACT

Polycyclic Aromatic Hydrocarbons (PAHs) are organic molecules which comprise the smallest particles of dust in the interstellar medium (ISM). Due to their broad/complex emission profiles, obtaining kinematics is a challenge with traditional methods, especially before the advent of the JWST. In this work we employ Principal Component Analysis (PCA) tomography to analyse JWST/NIRSpec IFU data of 3 nearby luminous infrared galaxies (LIRGs), namely, NGC 3256 N, NGC 3256 S and NGC 7469. We detect the signature of rotation in the second principal component of the 3.3 μm PAH feature in all three targets. We construct velocity maps from the principal components for the 3.3 μm PAH feature, Br β (2.625 μm) and molecular hydrogen, H₂ 1-0 S(1) (2.12 μm). We find that in each target, the PAHs qualitatively follow the rotation of the galaxy, consistent with the rotational signature derived from Br β and H₂. There are however some differences, with the PAH rotation in NGC 3256 N appearing at a different position angle, which suggest differences in the motion of the dust as compared to the gas. This kind of analysis opens a new window into this key component of the ISM.

Key words: galaxies: kinematics and dynamics – galaxies: ISM – techniques: spectroscopic

1 INTRODUCTION

Polycyclic Aromatic Hydrocarbons (PAHs) are molecules comprised of numerous carbon rings bonded with hydrogen and are the smallest particles of dust. PAH molecules are excited by UV photons from young stars (e.g. Tielens 2008) and therefore are thought to be excellent tracers of star-formation (e.g. Rigopoulou et al. 1999; Peeters et al. 2004; Shipley et al. 2016). These molecules are extremely abundant in galaxies, both locally (e.g. Brandl et al. 2006; Smith et al. 2007) and in the early universe (e.g. Spilker et al. 2023), playing an important role in the ISM (e.g. Bakes & Tielens 1994) and dominating the mid-IR spectra of galaxies. A missing diagnostic of this key component of the ISM are its kinematics.

Originating from the bending and stretching of C-H and C-C bonds, (e.g. Tielens 2008; Li 2020), PAH features have broad and complex profiles, consisting of multiple emission components (e.g. Rigopoulou et al. 2021; Draine & Li 2001). PAH profiles are significantly broader than any typical velocity signature in a galaxy, and thus measuring a velocity shift is challenging. Moreover, the intrinsic shape of a given PAH profile can vary based on the conditions of the ISM such as the hardness of the radiation field, the charge and the mass (e.g. Peeters et al. 2002; Candian & Sarre 2015; Shannon & Boersma 2019). This intrinsic broad shape also means there is no well-defined line centre that one can measure deviations from.

For these reasons, deriving kinematics from PAHs are extremely challenging to measure.

PAHs are a key component of the ISM and in particular in photo-dissociation regions (PDRs) (e.g. Hollenbach 1997), where PAHs are excited on the boundary between the ionised HII region and molecular gas (e.g. Andrews et al. 2015; Chown et al. 2023). Whether the motion of PAHs follow the molecular gas or ionised gas from stars is unknown, and in systems with strong outflows, the motion of PAHs is particularly interesting. This is especially true considering outflows are known affect the PAH population, resulting in altered ratios between different PAH bands (e.g. Beirão et al. 2015; García-Bernete et al. 2022b, García-Bernete submitted.).

Following Gorski et al. (2023) and utilising the method outlined in Steiner et al. (2009), we apply Principal Component Analysis (PCA) tomography to identify signatures of PAH kinematics from the data where traditional methods (such as modelling the profile with a Gaussian) are not suitable for the reasons outlined above.

PCA is a method of dimensionality reduction by transforming the data into a new coordinate system of uncorrelated principal components, each of which describe decreasing variance within the data. PCA has been widely used in astronomy, such as with Spitzer spectra (e.g. Wang et al. 2011; Hurley et al. 2012; Sidhu et al. 2022), as it provides a blind technique that can extract information from higher dimensions in the data. When applied to data cubes which contain two spatial dimensions and a spectral dimension, the PCA reduction extracts eigenvectors (in this case eigenspectra) using the information contained in the spatial axes. This allows spectral signals that

* E-mail: fergus.donnan@physics.ox.ac.uk

correlate with some spatial distribution, that may be hidden in the data, to be uncovered (e.g. Meier & Turner 2005; Steiner et al. 2009; Ricci et al. 2011; Gorski et al. 2023).

By isolating emission features in the data, kinematic signatures such as rotation or inflowing/outflowing material can be revealed, typically as the second or third principal component (e.g. Gorski et al. 2023).

In this letter we first summarise the technique of Steiner et al. (2009) in Section 3 before applying the technique to JWST/NIRSpec data of three targets (See Donnan et al. 2024, for more details) in Section 4. We apply PCA to the 3.3 μm PAH, Br β (2.62 μm), H $_2$ (2.12 μm) and compare the kinematics of each.

2 JWST/NIRSPEC DATA

We use NIRSpec IFU data from Director’s Discretionary Early Release Science Program 1328 (PI: Lee Armus & Aaron Evans) of three galaxies, NGC 3256 N, NGC 3256 S and NGC 7469. We use the data presented in Donnan et al. (2024), reduced with modifications to the default pipeline as described in García-Bernetete et al. (2024); Pereira-Santaella et al. (2024b).

NGC 3256 is a late-stage merger of two galaxies, where each nucleus was observed separately. The northern component is a near face-on spiral hosting a star-forming nucleus (NGC 3256 N, Sakamoto et al. 2014; Lira et al. 2008), while the southern component is an edge-on spiral hosting an obscured AGN (NGC 3256 S, Ohya et al. 2015; Pereira-Santaella et al. 2024b; Donnan et al. 2024). Both nuclei drive molecular outflows (Sakamoto et al. 2014; Pereira-Santaella et al. 2024b).

NGC 7469 is a barred spiral galaxy with a type 1 AGN residing within a starburst ring (e.g. Osterbrock & Martel 1993; Díaz-Santos et al. 2007; García-Bernetete et al. 2022a; Lai et al. 2022, 2023). For a plot of the field-of-view of the NIRSpec observations for each target, see Fig. 6 of Donnan et al. (2024).

3 PRINCIPAL COMPONENT ANALYSIS TOMOGRAPHY

3.1 PCA

Before applying the PCA technique, we first prepare the data cubes by isolating the emission feature within the cube and subtracting the continuum. We use a simple local continuum by fitting a straight line between either side of the emission feature. This produces a cube with the only the emission feature present. Additionally we subtract the mean flux at each wavelength to normalise the data cube, a standard practice for PCA. The following summarises the technique described in Steiner et al. (2009).

The resulting data cube has a total of m spectral pixels and $n = \mu \times \nu$ spatial pixels, where μ and ν are the number of pixels in x and y respectively. From this we additionally reorganise the data cube, $\mathbf{I}_{x,y,\lambda}$ by stacking the spatial dimensions, x and y , into a single coordinate, β where

$$\beta = \mu(x - 1) + y. \quad (1)$$

The reorganised data cube, $\mathbf{I}_{\beta,\lambda}$ is transformed using

$$\mathbf{T}_{\beta,k} = \mathbf{I}_{\beta,\lambda} \cdot \mathbf{E}_{\lambda,k} \quad (2)$$

where $\mathbf{T}_{\beta,k}$ is the transformed data which can be mapped back to the original spatial dimensions $\mathbf{T}_{x,y,k}$, using equation (1). These are the tomograms for each principal component, k , where $k = 1$ gives the first principal component with subsequent components describing

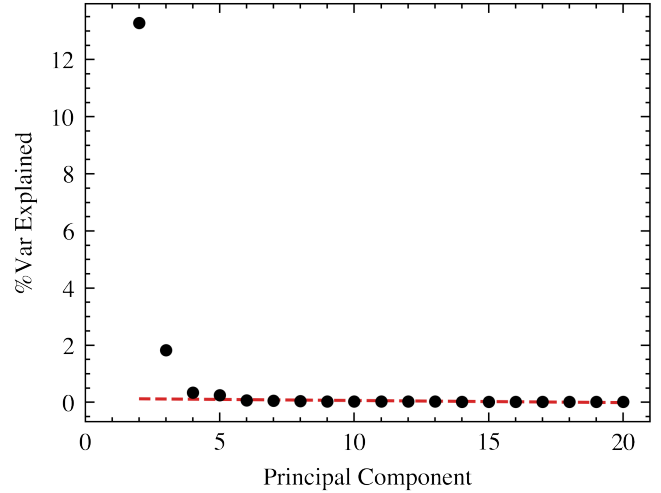


Figure 1. Scree test for the PCA applied to Br β for NGC 3256 N, which shows the first three principal components are significant. The 1st component explains 83.5% of the variance and appears of the scale. The red dashed line shows a linear fit the the higher order components where no useful information is contained.

decreasing variance within the data. $\mathbf{E}_{\lambda,k}$ contains the eigenvectors of each component, k , which in this case we call eigenspectra, as these are functions of wavelength, λ . The tomogram, $T_{x,y,k}$, therefore describes the spatial correlation of its corresponding eigenspectrum and can thus be used to reveal signals hidden in the data that are spatially correlated.

To establish if the components are useful, we can perform a Scree test (Cattell 1966), which provides a measure of the variance explained by each principal component. This is shown in Fig. 1 for Br β (2.62 μm) in NGC 3256 N and demonstrates that the first three components significantly above the point where the plot levels off.

We demonstrate this in Fig. 2, with Br β (2.62 μm) emission in NGC 3256 N, where the first principal component describes 83.5% of the variance of the data. Physically this corresponds to restframe emission of the line as the eigenspectrum shows a narrow line profile, centred on its restframe wavelength.

The second component contains 13.3% of the variance in the data and appears to contain information about the rotation of the gas. Here the eigenspectrum shows excess flux redwards of the line centre and a lack of flux bluewards and thus describes a redshifted emission line. The tomogram shows the strength of this eigenspectrum across the galaxy where the greater positive weight suggests more redshifted emission while negative strengths describe the inverse i.e blueshifted emission. The second principal component here is consistent with the known rotation of this galaxy (Crespo Gómez et al. 2021). Moreover, the wavelength where the eigenspectrum crosses from negative to positive is consistent with the restframe wavelength of the line and spatially coincides with the position of the nucleus. It is worth noting the tomogram is not a velocity map (see section 3.2).

The third component describes 1.8% of the variance, and shows an eigenspectrum with excess flux in the wings where the tomogram is strongly positive and an excess flux with a narrow profile where the tomogram is strongly negative. This contributes more extreme values of velocity to the total velocity field. Subsequent principal components will have a diminishing contribution to the velocity field as the Scree test in Fig. 1 demonstrates. We show the effect of adding different numbers of principal components in the Supplementary Material, where components above three contribute minimally.

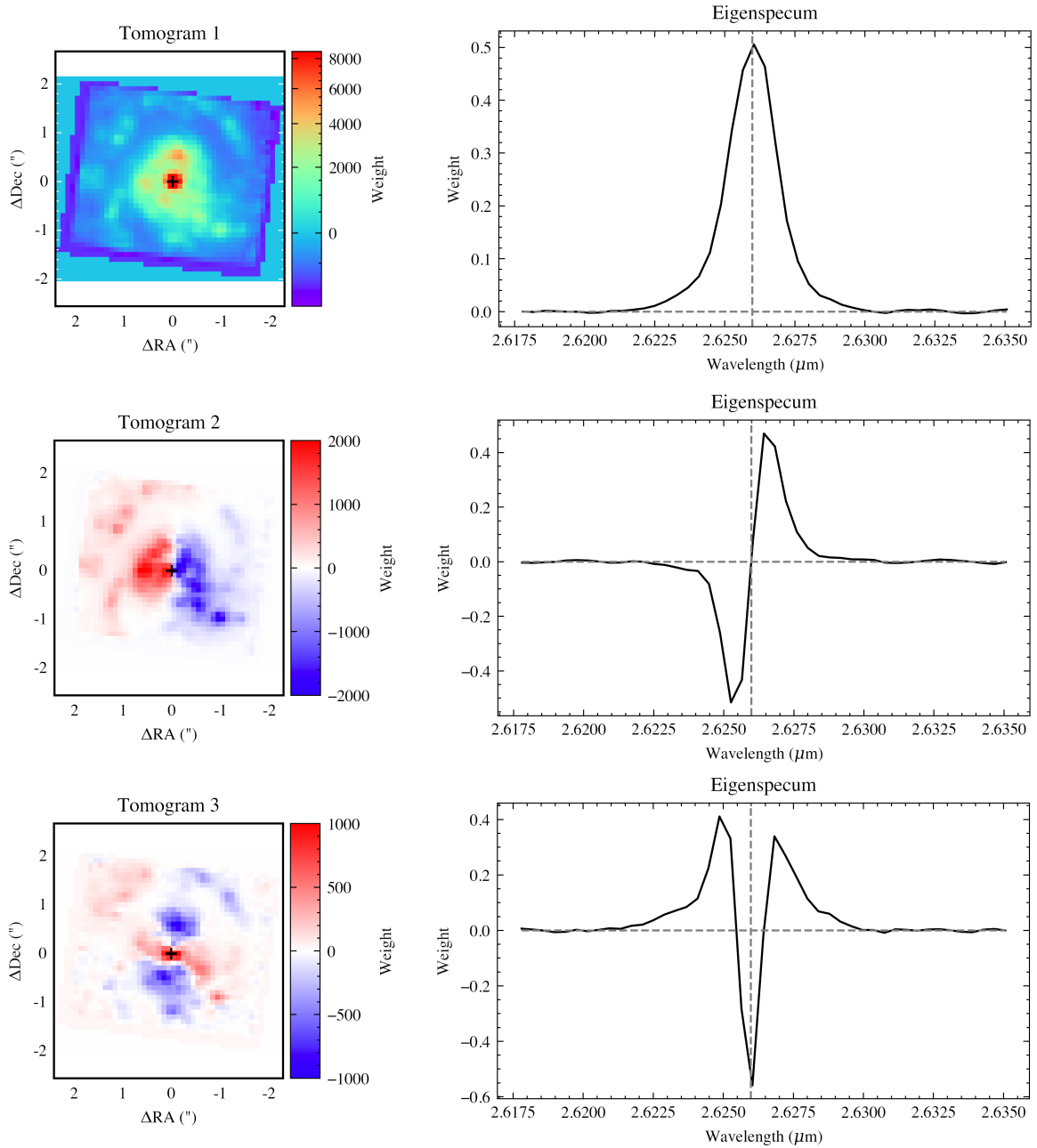


Figure 2. The first three principal components for a data cube of Br β ($2.62 \mu\text{m}$) of NGC 3256 N. The left panels show the tomograms of each component which describes the spatial intensity of each eigenspectrum. The black crosses show the peak continuum position at this wavelength. The right panels show the eigenspectrum of each principal component. The horizontal dashed lines show where the weight is zero and the vertical dashed lines show the kinematic centre, determined by the peak wavelength of the first principal component. The first component describes the rest frame emission, while the second captures rotation of the gas and the third captures variations in the velocity dispersion.

3.2 Recovering Velocity Maps

One can reconstruct the original data cube by summing the eigenspectra where each is weighted by its corresponding tomogram. As the majority of the principal components simply describe noise in the data, reconstructing only using the first few components produces a data cube with less noise than the original data. A velocity map can then be constructed.

We reconstruct a data cube using only the first five components to obtain a velocity map. With this number of components, we are sure to capture all of the kinematics without the noise contained in the higher order components.

As the first component describes the restframe emission, we take its eigenspectrum as a template for the rest profile of the emission feature. For each spaxel in the reconstructed cube, we calculate the wavelength (and thus velocity) shift required to match the restframe template to the emission for that spaxel. This provides a velocity for each spaxel and thus produces a velocity map.

We compare the inferred velocity map against a more traditional method of fitting a Gaussian to each spaxel. We do this for all the emission lines used in this work and investigate the effect of the number of principal components in the reconstructed cube. This can be found in more detail in the Supplementary Material. We find that

the PCA recovered map is typically consistent with the traditional method with at least the first three components required. For the PAH emission, we find that typically the first two components are sufficient.

4 PAH KINEMATICS

4.1 PCA of PAH Emission

As outlined above, the PCA technique can isolate kinematic signatures by using the spatial distribution of the emission, without requiring any a priori knowledge of the emission profile. This technique is therefore well suited to detect/measure any kinematic signatures of the PAHs.

We focus on the $3.3\ \mu\text{m}$ PAH as this feature is not heavily blended with other PAHs, is fairly symmetrical and has a high spatial resolution owing to NIRSPEC observations. This feature is therefore ideal for this initial study of the kinematics of PAH features. Other PAH features, such as the $6.2\ \mu\text{m}$ or $11.3\ \mu\text{m}$ features, will be explored in future works.

Before the PCA analysis, we mask the $\text{P}\delta$ ($3.296\ \mu\text{m}$) line and subtract a local continuum to isolate the PAH feature. Fig. 3 shows the first two tomograms where the first describes the restframe emission and contains 99.9% of the variance. The second principal component shows evidence of kinematics with the eigenspectrum showing excess flux redwards and a lack of flux bluewards, with the corresponding tomogram showing a gradient from positive to negative weights from east to west. The second component contains only 0.04% of the variance which highlights how buried the kinematic signature is within the data. Unlike $\text{Br}\beta$, the 3rd principal component does not contain any useful information as more subtle changes in the profile, which would be captured by higher order components, are likely too difficult to detect in the data, unlike emission lines.

To demonstrate how small the velocity shifts are compared to the width of the PAH features, we plot the average PAH profile for the approaching and receding sides of the galaxy in Fig. 4. This is calculated by taking the average of the emission feature in pixels where the second tomogram is only positive (receding) or only negative (approaching).

For each of the three targets we apply the PCA method to $\text{Br}\beta$ ($2.62\ \mu\text{m}$) to trace the kinematics of young stars, H_2 1-0 S(1) ($2.12\ \mu\text{m}$) to trace molecular gas, and the $3.3\ \mu\text{m}$ PAH to trace dust, as discussed in the previous section. We then compare the kinematics of these tracers.

Fig. 5 shows the velocity maps for each target with each emission feature. Before applying the PCA method to the PAH cubes, we smooth each channel with a Gaussian filter with a $\sigma = 1$ pixel. This is due to the low signal to noise of the kinematics in the data. We additionally do this for the $\text{Br}\beta$ and H_2 lines for NGC 7469, as the signal to noise is lower for this target. We also mask the point source in NGC 7469 as the PSF is particularly strong for this target, which introduces ‘‘wiggles’’ into individual pixels near the centre (e.g. [Perna et al. 2023](#)), disrupting the PCA decomposition.

5 DISCUSSION

For all three targets, the PAHs show clear signatures of kinematics and qualitatively follow the rotation of the galaxy. We calculate a Pearson correlation coefficient between the velocity maps of the various tracers to quantify how well the different emission features trace the same kinematics. This is shown in Table. 1.

Table 1. Velocity Map Correlations. The 4th column shows the Pearson correlation coefficient between the two given maps.

Galaxy	Correlation	N_{spaxels}	ρ
NGC 3256 N	$\text{Br}\beta$ vs H_2	1490	0.89
NGC 3256 N	PAH(3.3) vs H_2	1490	0.24
NGC 3256 N	PAH(3.3) vs $\text{Br}\beta$	1650	0.25
NGC 3256 S	$\text{Br}\beta$ vs H_2	1478	0.75
NGC 3256 S	PAH(3.3) vs H_2	1494	0.68
NGC 3256 S	PAH(3.3) vs $\text{Br}\beta$	1597	0.60
NGC 7469	$\text{Br}\beta$ vs H_2	2193	0.86
NGC 7469	PAH(3.3) vs H_2	2193	0.74
NGC 7469	PAH(3.3) vs $\text{Br}\beta$	2426	0.80

NGC 7469 shows the strongest agreement between the gas tracers and the PAHs both qualitatively as well as having the highest Pearson correlation coefficients. This is despite the presence of a nuclear outflow (e.g. [García-Bernete et al. 2022b](#); [Armus et al. 2023](#)), although the outflow is most prominent in the ionised phase. For a more detailed kinematic analysis for this target see [Bianchin et al. \(2023\)](#); [U et al. \(2022\)](#).

While the other two targets also broadly show agreement, there are some clear differences between the velocity maps. For NGC 3256 S, the H_2 maps correlates well with the PAHs however $\text{Br}\beta$ shows a peculiar velocity field and thus the correlation is worse. This is in agreement with the maps shown in [Pereira-Santaella et al. \(2024b,a\)](#), however the reason for the unusual velocity field of $\text{Br}\beta$ is unclear. It is also worth noting that the velocity map of H_2 is not dominated by the strong/collimated molecular outflow driven by the obscured AGN (e.g. [Sakamoto et al. 2014](#); [Pereira-Santaella et al. 2024b](#)). This is likely due to the high inclination of the galaxy where the line of sight velocity is dominated by rotation whereas the radial component of the outflow will be relatively weak.

For NGC 3256 N, the kinematic position angle of the PAH velocity map appears to be different to $\text{Br}\beta$ and H_2 , resulting in a poorer correlation, which may suggest a warp in the inner disk. This can be clearly seen in the eigenspectrum of the 2nd component in Fig. 3, which is dominated by the rotation. In addition there appears to be more blueshifted emission which may be due to the rest emission being estimated incorrectly. As we used the 1st principal component as the rest emission, this provides an average over the field of view. If for example, more of one side of the disk was visible in the field of view, this would shift the rest emission as given by the 1st principal component. In this work however, this is not a likely explanation as the nuclei are centered in the observations.

6 CONCLUSIONS

In this letter we have demonstrated how the kinematics of PAHs can be inferred using PCA tomography. Our main findings are

- We demonstrate the technique of PCA tomography with JWST/NIRSPEC data, where the second component isolates the rotation of the gas while the third corresponds to the velocity dispersion.
- By applying the PCA technique, we detect a kinematic signature of the $3.3\ \mu\text{m}$ PAH feature in all three targets.
- By reconstructing a velocity map, we find the PAH emission to follow the rotation of the galaxy, with consistent values of velocity.

With this technique, future work exploring the kinematics of other PAH features, by incorporating MIRI MRS data, will provide a new window into this crucial component of the ISM.

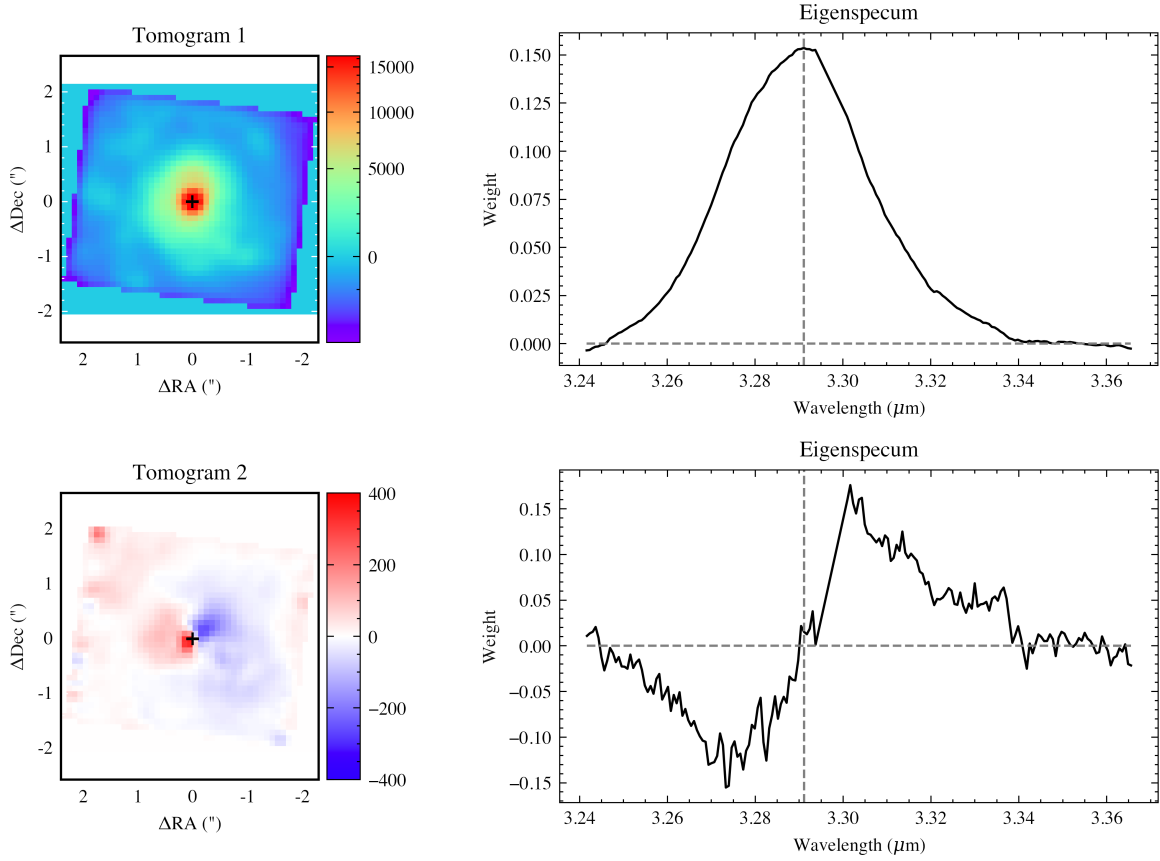


Figure 3. First two principal components of the $3.3 \mu\text{m}$ PAH in NGC 3256 N. The first component describes the restframe emission while the second describes kinematics of the PAHs. The left panels show the tomograms of each principal component, with the position of the continuum peak shown with a black cross. The right panels show the corresponding eigenspectra.

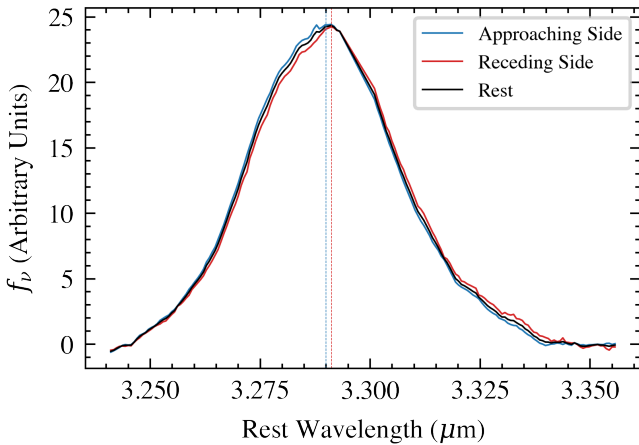


Figure 4. Average $3.3 \mu\text{m}$ PAH profiles for the approaching, receding and rest frame emission for NGC 3256 S. The vertical dashed lines show the mean wavelength of approaching and receding profiles. This plot highlights how small the velocity shifts are compared to the width of the emission feature, prompting the need to employ techniques such as PCA tomography.

ACKNOWLEDGEMENTS

The authors are grateful to the DD-ERS team (Program 1328, PI: Lee Armus & Aaron Evans) for the observing program with a zero-exclusive-access period. FRD acknowledges support from

STFC through grant ST/W507726/1. DR and IGB acknowledge support from STFC through grant ST/S000488/1 and ST/W000903/1.

DATA AVAILABILITY

All the data used in this work is publicly available as part of DD-ERS Program 1328, downloadable from the [MAST archive](#).

REFERENCES

- Andrews H., Boersma C., Werner M. W., Livingston J., Allamandola L. J., Tielens A. G. G. M., 2015, *ApJ*, **807**, 99
- Armus L., et al., 2023, *ApJ*, **942**, L37
- Bakes E. L. O., Tielens A. G. G. M., 1994, *ApJ*, **427**, 822
- Beirão P., et al., 2015, *Monthly Notices of the Royal Astronomical Society*, **451**, 2640
- Bianchin M., et al., 2023, *arXiv e-prints*, p. arXiv:2308.00209
- Brandl B. R., et al., 2006, *ApJ*, **653**, 1129
- Candian A., Sarre P. J., 2015, *MNRAS*, **448**, 2960
- Cattell R. B., 1966, *Multivariate Behavioral Research*, **1**, 245
- Chown R., et al., 2023, *arXiv e-prints*, p. arXiv:2308.16733
- Crespo Gómez A., Piqueras López J., Arribas S., Pereira-Santaella M., Colina L., Rodríguez del Pino B., 2021, *A&A*, **650**, A149
- Díaz-Santos T., Alonso-Herrero A., Colina L., Ryder S. D., Knapen J. H., 2007, *ApJ*, **661**, 149
- Donnan F. R., García-Bernete I., Rigopoulou D., Pereira-Santaella M., Roche P. F., Alonso-Herrero A., 2024, *MNRAS*,
- Draine B. T., Li A., 2001, *ApJ*, **551**, 807

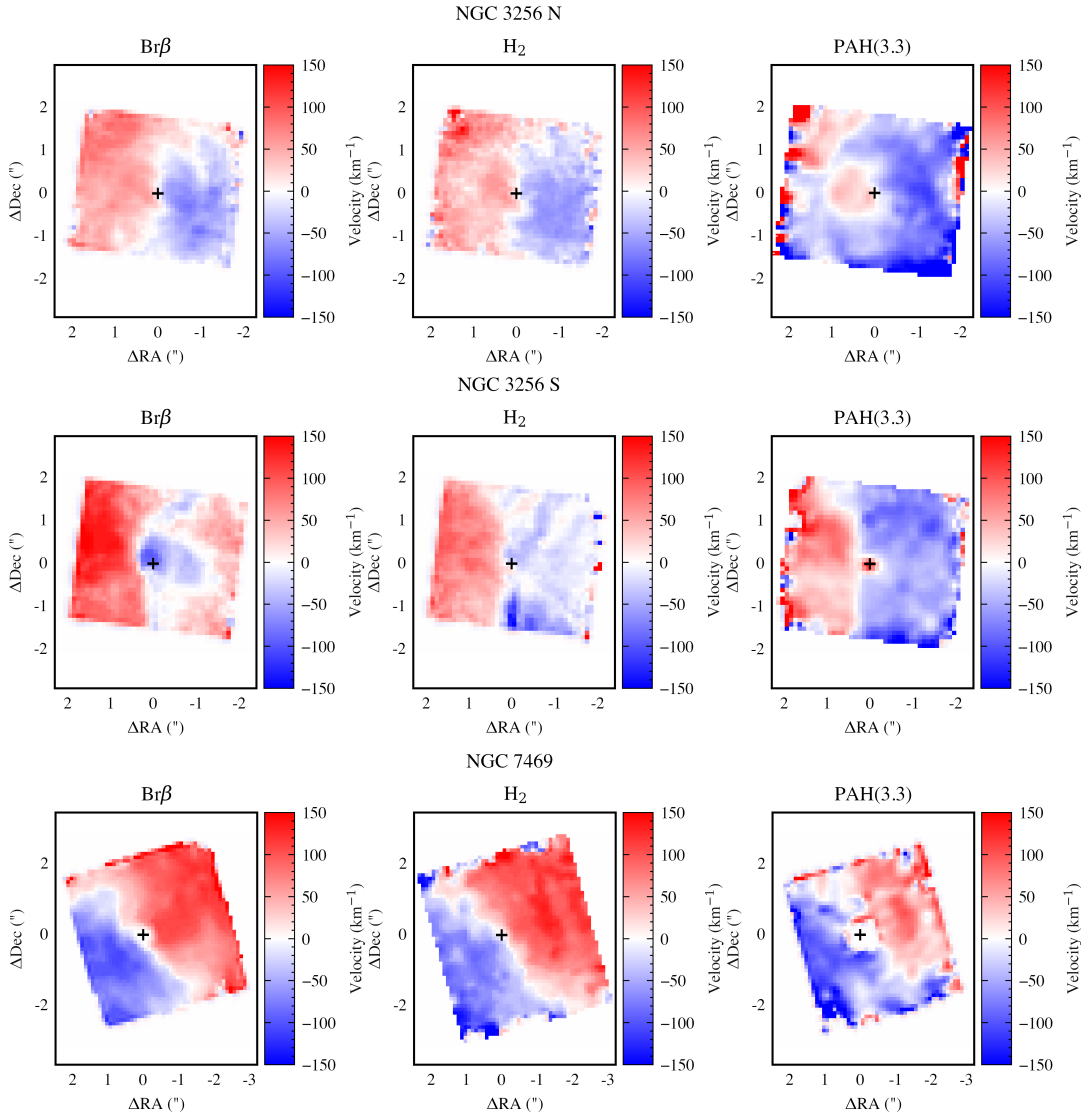


Figure 5. Velocity maps inferred from the PCA decomposition for the three targets. In each case the velocity map is constructed using the first five principal components. The left most panels show Br β ($2.625 \mu\text{m}$), the middle panels show H $_2$ 1-0 S(1) ($2.12 \mu\text{m}$) and the right panels show the $3.3 \mu\text{m}$ PAH maps. For all the maps, the black cross denotes the continuum peak position at the wavelengths of the emission line.

García-Bernete I., Rigopoulou D., Alonso-Herrero A., Pereira-Santaella M., Roche P. F., Kerkeni B., 2022a, *MNRAS*, **509**, 4256
 García-Bernete I., et al., 2022b, *A&A*, **666**, L5
 García-Bernete I., et al., 2024, *A&A*, **681**, L7
 Gorski M. D., et al., 2023, *A&A*, **670**, A70
 Hollenbach D., 1997, pp 181–198
 Hurley P. D., Oliver S., Farrah D., Wang L., Efstathiou A., 2012, *MNRAS*, **424**, 2069
 Lai T. S. Y., et al., 2022, *ApJ*, **941**, L36
 Lai T. S. Y., et al., 2023, *arXiv e-prints*, p. [arXiv:2307.15169](https://arxiv.org/abs/2307.15169)
 Li A., 2020, *Nature Astronomy*, **4**, 339
 Lira P., Gonzalez-Corvalan V., Ward M., Hoyer S., 2008, *MNRAS*, **384**, 316
 Meier D. S., Turner J. L., 2005, *ApJ*, **618**, 259
 Ohyama Y., Terashima Y., Sakamoto K., 2015, *ApJ*, **805**, 162
 Osterbrock D. E., Martel A., 1993, *ApJ*, **414**, 552
 Peeters E., Hony S., Van Kerckhoven C., Tielens A. G. G. M., Allamandola L. J., Hudgins D. M., Bauschlicher C. W., 2002, *A&A*, **390**, 1089
 Peeters E., Spoon H. W. W., Tielens A. G. G. M., 2004, *ApJ*, **613**, 986
 Pereira-Santaella M., et al., 2024a, *arXiv e-prints*, p. [arXiv:2404.16641](https://arxiv.org/abs/2404.16641)
 Pereira-Santaella M., González-Alfonso E., García-Bernete I., García-Burillo S., Rigopoulou D., 2024b, *A&A*, **681**, A117

Perna M., et al., 2023, *A&A*, **679**, A89
 Ricci T. V., Steiner J. E., Menezes R. B., 2011, *ApJ*, **734**, L10
 Rigopoulou D., Spoon H. W. W., Genzel R., Lutz D., Moorwood A. F. M., Tran Q. D., 1999, *AJ*, **118**, 2625
 Rigopoulou D., et al., 2021, *MNRAS*, **504**, 5287
 Sakamoto K., Aalto S., Combes F., Evans A., Peck A., 2014, *ApJ*, **797**, 90
 Shannon M. J., Boersma C., 2019, *ApJ*, **871**, 124
 Shipley H. V., Papovich C., Rieke G. H., Brown M. J. I., Moustakas J., 2016, *ApJ*, **818**, 60
 Sidhu A., Bazely J., Peeters E., Cami J., 2022, *MNRAS*, **511**, 2186
 Smith J. D. T., et al., 2007, *ApJ*, **656**, 770
 Spilker J. S., et al., 2023, *Nature*, **618**, 708
 Steiner J. E., Menezes R. B., Ricci T. V., Oliveira A. S., 2009, *MNRAS*, **395**, 64
 Tielens A. G. G. M., 2008, *ARA&A*, **46**, 289
 U V., et al., 2022, *ApJ*, **940**, L5
 Wang L., Farrah D., Connolly B., Connolly N., Lebouteiller V., Oliver S., Spoon H., 2011, *MNRAS*, **411**, 1809

This paper has been typeset from a \LaTeX file prepared by the author.

The Kinematics of Polycyclic Aromatic Hydrocarbons (PAHs) in Galaxies from Principal Component Analysis (PCA) tomography of JWST/NIRSpec data: Supplementary Material

Fergus R. Donnan, ¹* Dimitra Rigopoulou,^{1,2} Ismael García-Bernete ¹

¹*Department of Physics, University of Oxford, Keble Road, Oxford, OX1 3RH, UK*

²*School of Sciences, European University Cyprus, Diogenes street, Engomi, 1516 Nicosia, Cyprus*

Accepted XXX. Received YYY; in original form ZZZ

1 NUMBER OF PCA COMPONENTS

We described in the main text how we generate velocity maps from the components obtained from the PCA decomposition. In this section we demonstrate how the inferred velocity map changes based on the number of components included in the reconstructed cube. We then compare this to a traditional method of modelling the line profile of each spaxel in the original data cube. We do this for each of the emission lines.

For the traditional method we fit a Gaussian to the continuum subtracted spectra from each pixel. The velocity is inferred by measuring the difference in wavelength of the centre of the fitted Gaussian to the restframe centre wavelength of the emission line.

We first demonstrate this for Br β in NGC 3256 N. We find that the first two principal components contain the vast majority of the information about the velocity field, with subsequent principal components contain ever decreasing information. The higher order components appear to contain information about the more extreme values of velocity in the field which presents as smaller variations in the line profiles. We show in Fig. 1, the comparison between the traditional method and the PCA reconstructed velocity map from different number of components. The PCA velocity maps from just the first two components appears too “flat”, while including the third component shows a closer match to the traditional method. Beyond the third component, very little changes as most of the information is contained in the first three components, as learnt from the Scree test.

We additionally show the same comparison for the remaining lines/PAHs used in this work in Figs. 2, 3, 4, 5, 6, 7, 8, 9.

2 ADDITIONAL PCA PLOTS

In Fig. 10, 11, 12, 13, 14, 15, 16 we show the PCA decomposition for the other emission features in this work.

This paper has been typeset from a T_EX/L^AT_EX file prepared by the author.

arXiv:2405.13669v1 [astro-ph.GA] 22 May 2024

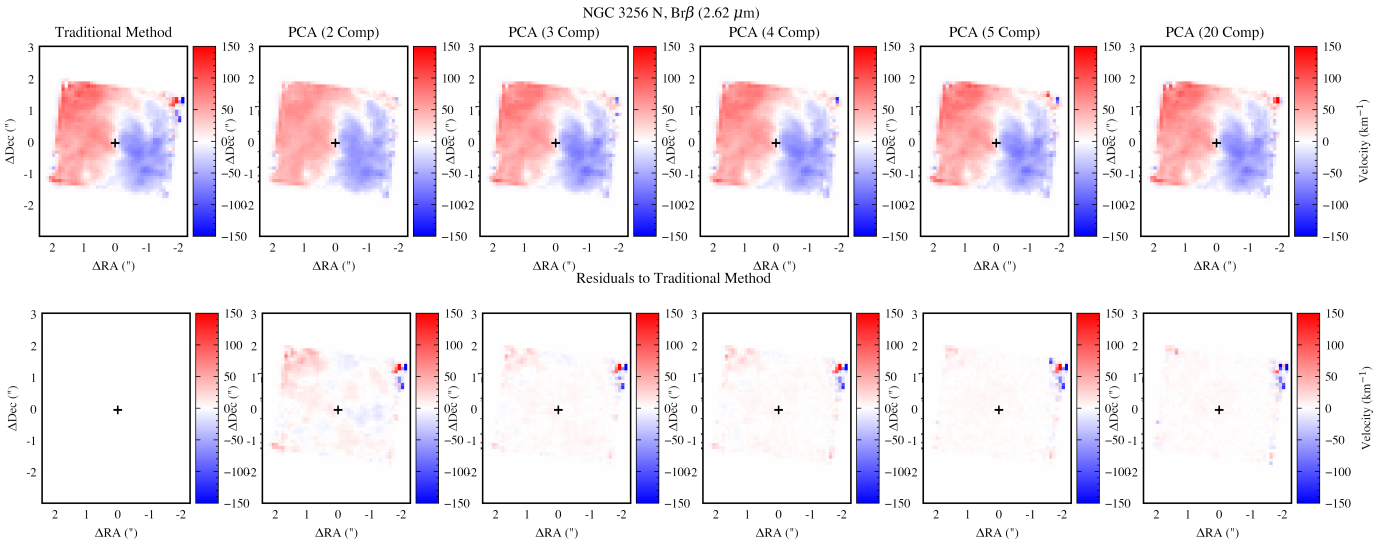


Figure 1. Comparison between the inferred velocity maps from the traditional method of fitting a Gaussian to each spaxel and those from the PCA, with different number of components. The top panels show the velocity maps while the lower panels show the residuals to the traditional method.

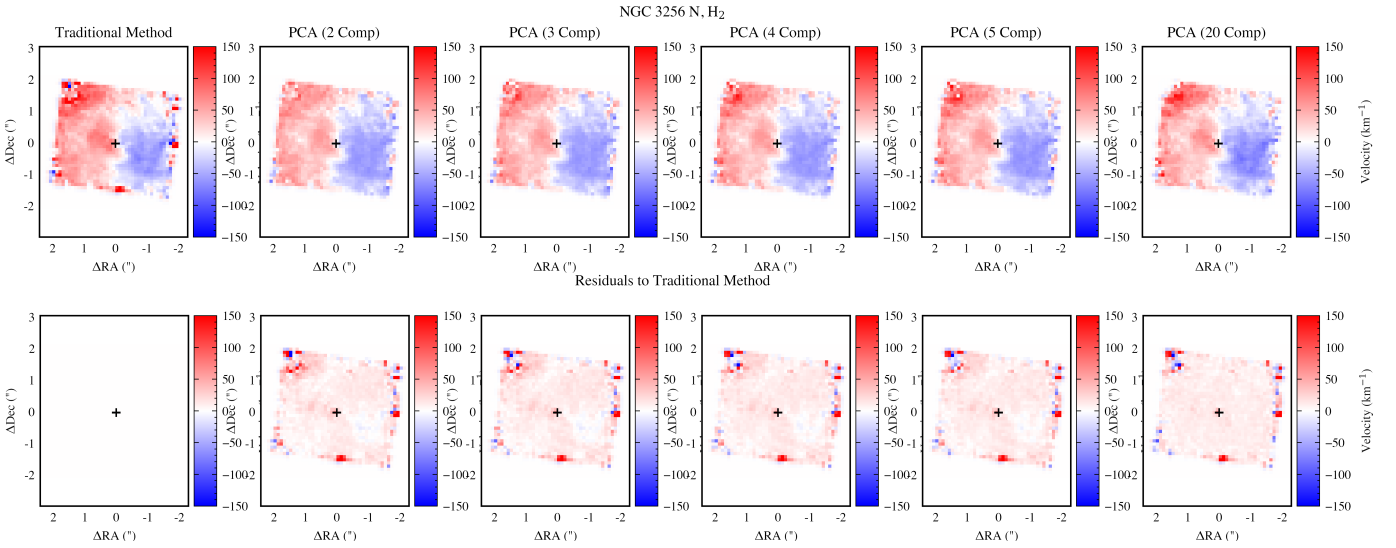


Figure 2. Same as Fig. 1 but for NGC 3256 N H $_2$.

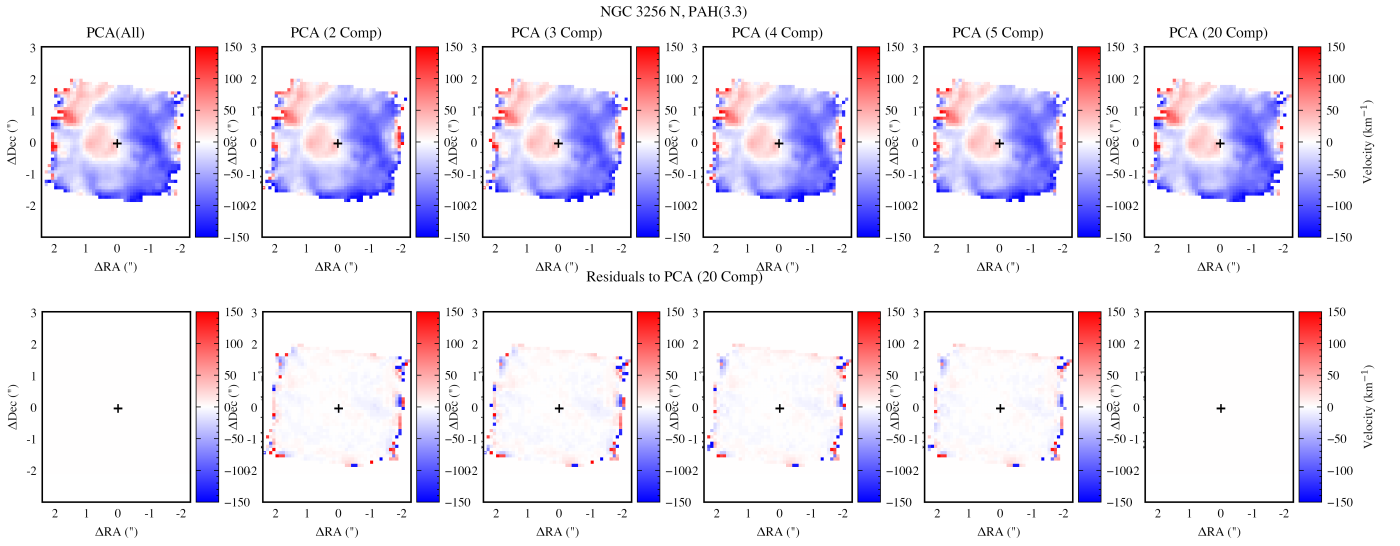


Figure 3. Same as Fig. 1 but for the $3.3\ \mu\text{m}$ PAH emission in NGC 3256 N. As the traditional method is not suitable for PAHs, we take the residuals relative to the 20 component PCA map.

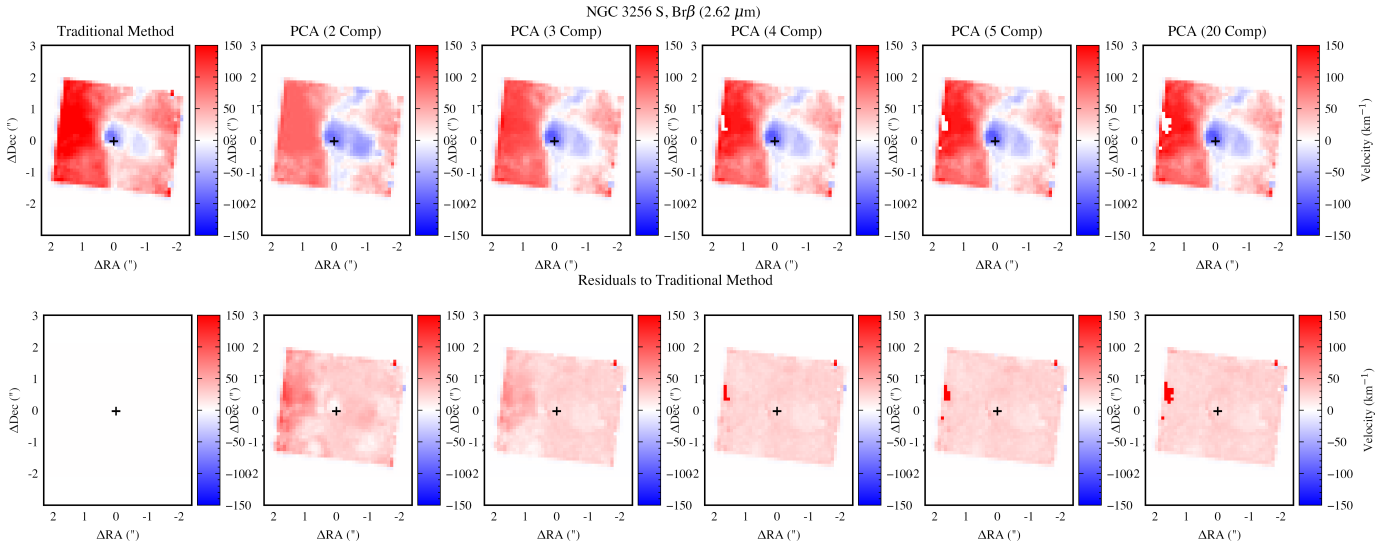


Figure 4. Same as Fig. 1 but for NGC 3256 S Br β .

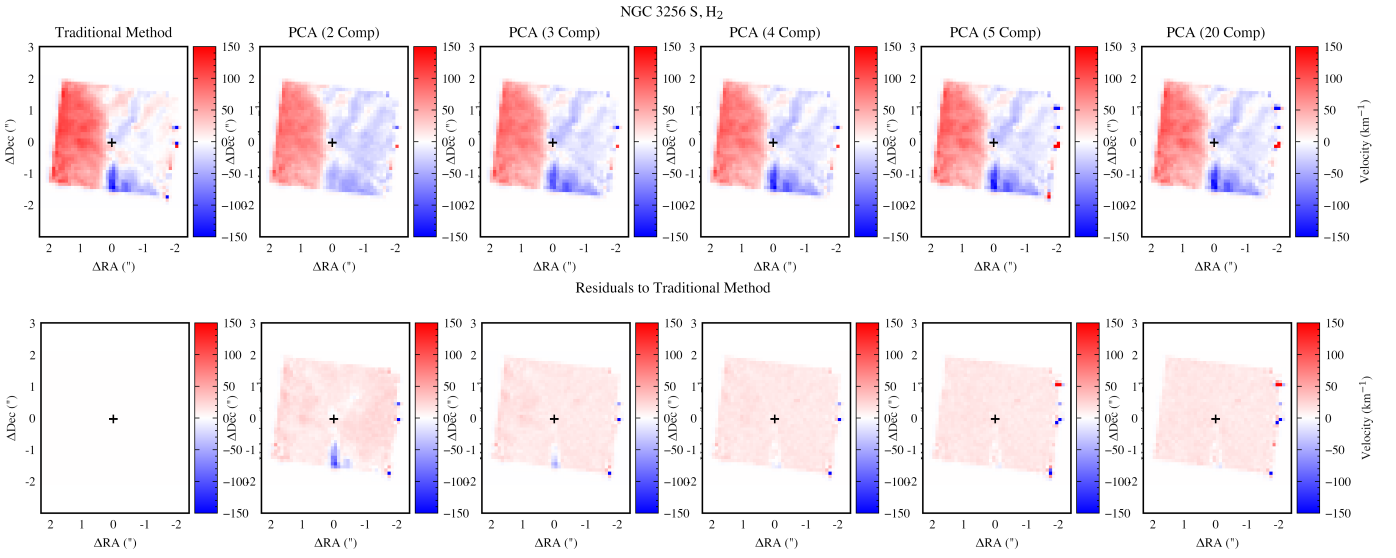


Figure 5. Same as Fig. 1 but for NGC 3256 S H₂.

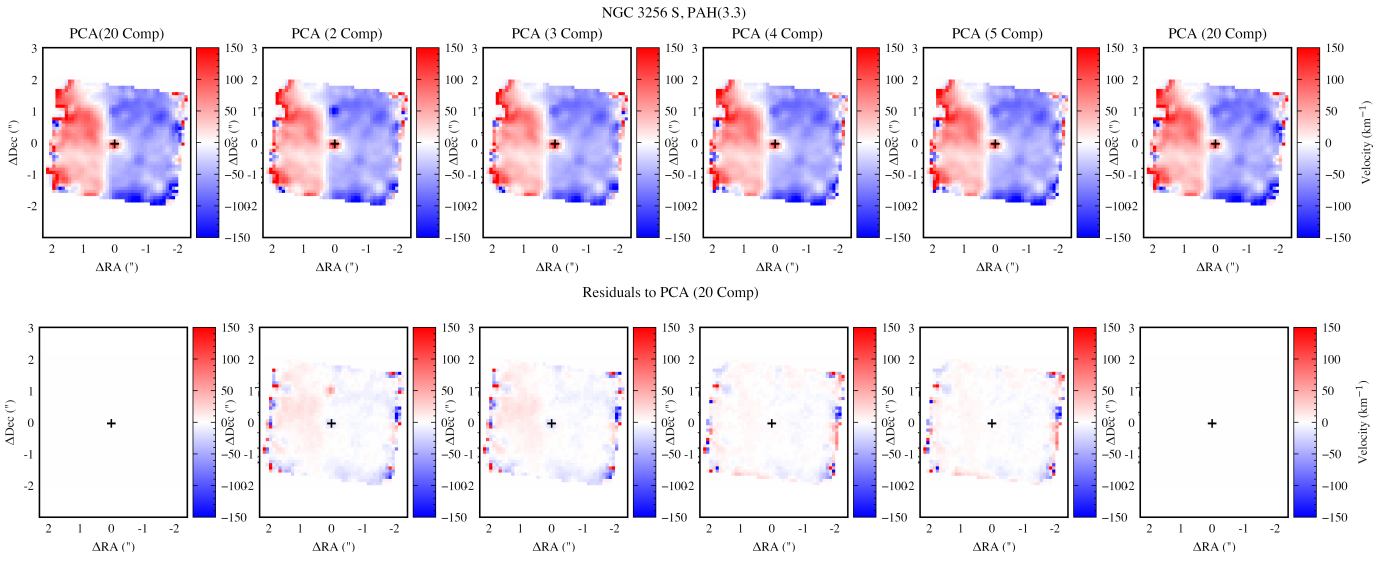


Figure 6. Same as Fig. 1 but for the 3.3 μm PAH emission in NGC 3256 S. As the traditional method is not suitable for PAHs, we take the residuals relative to the 20 component PCA map.

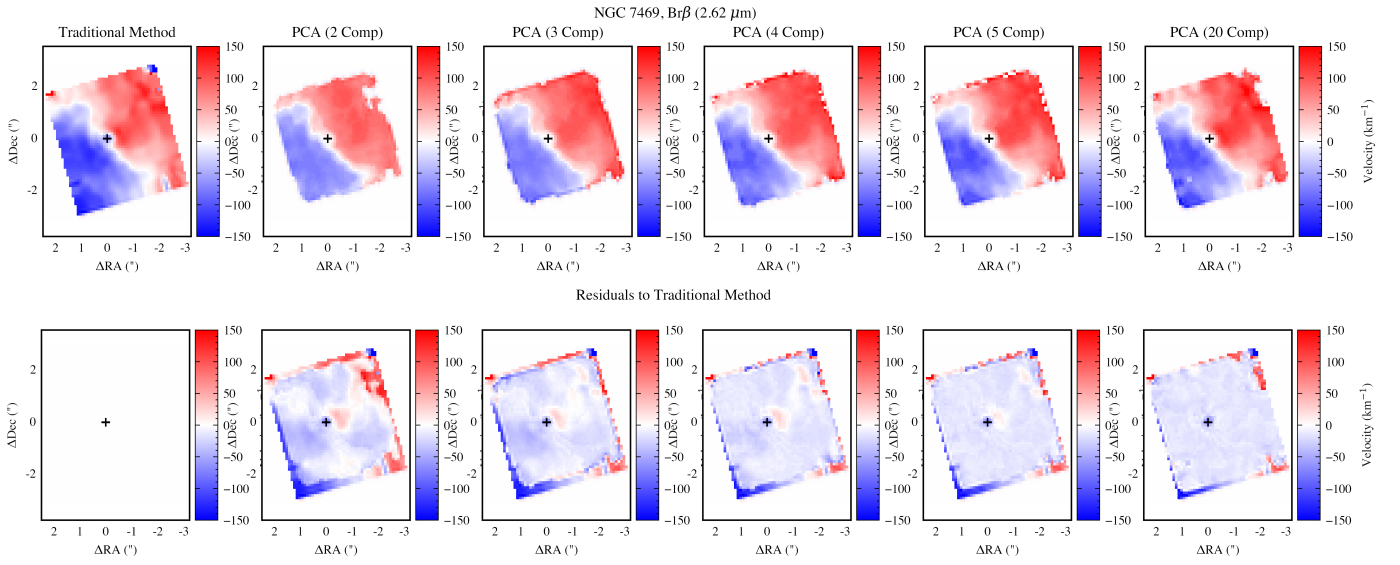


Figure 7. Same as Fig. 1 but for NGC 7469 Br β .

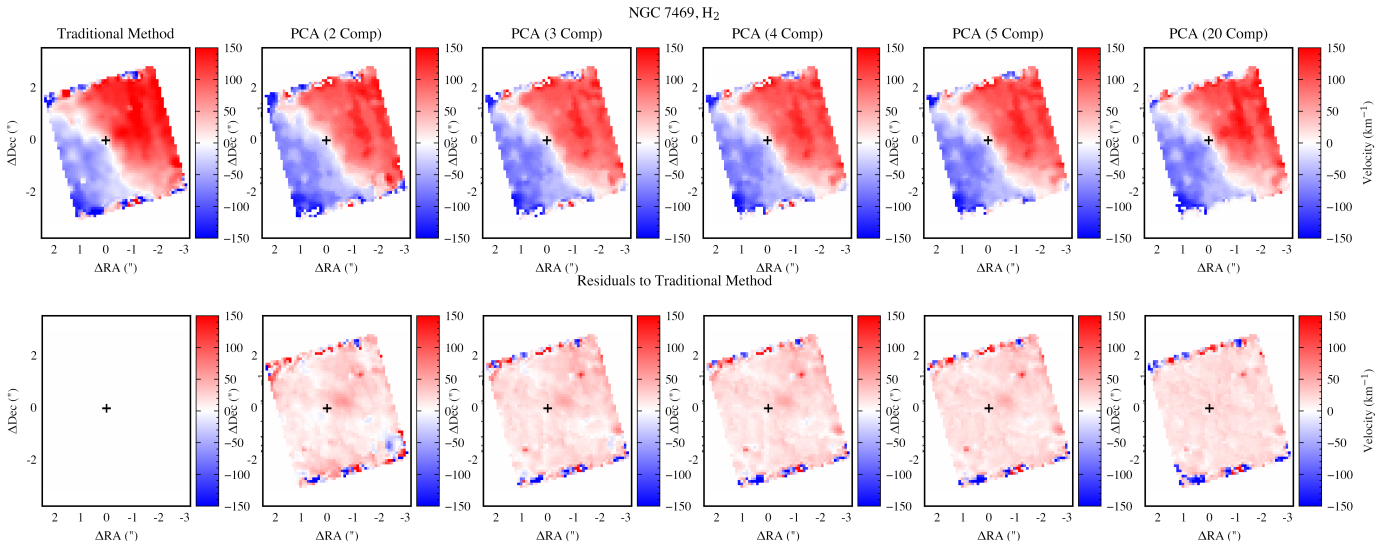


Figure 8. Same as Fig. 1 but for NGC 7469 H $_2$.

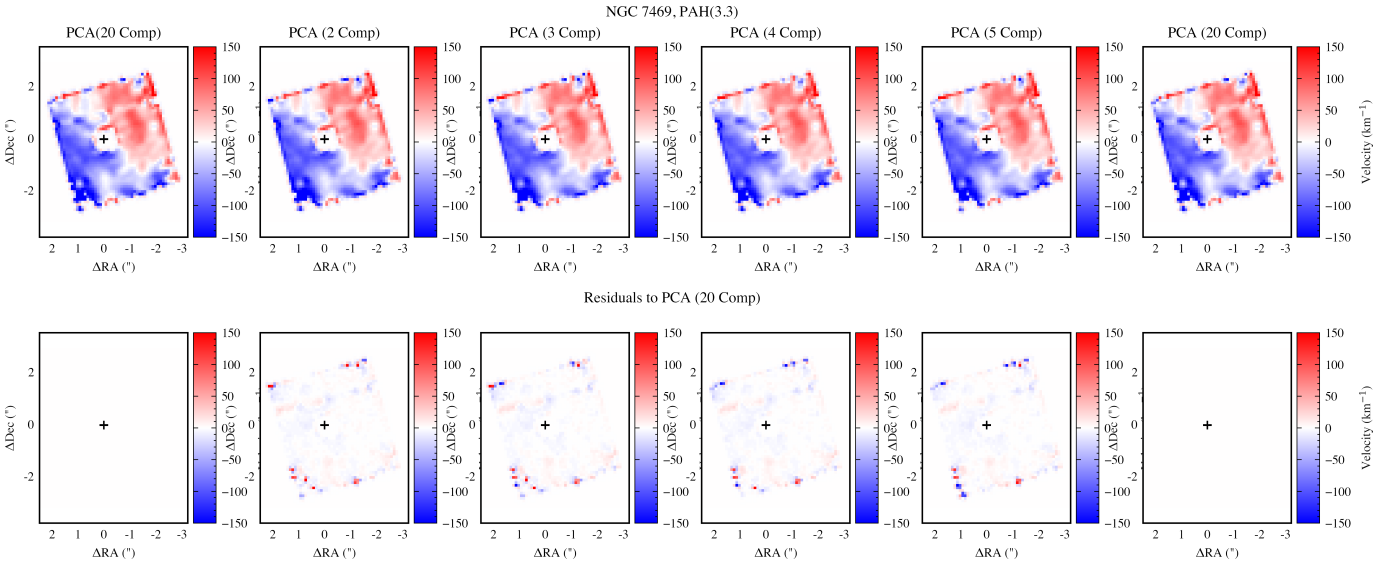


Figure 9. Same as Fig. 1 but for the 3.3 μm PAH emission in NGC 7469. As the traditional method is not suitable for PAHs, we take the residuals relative to the 20 component PCA map.

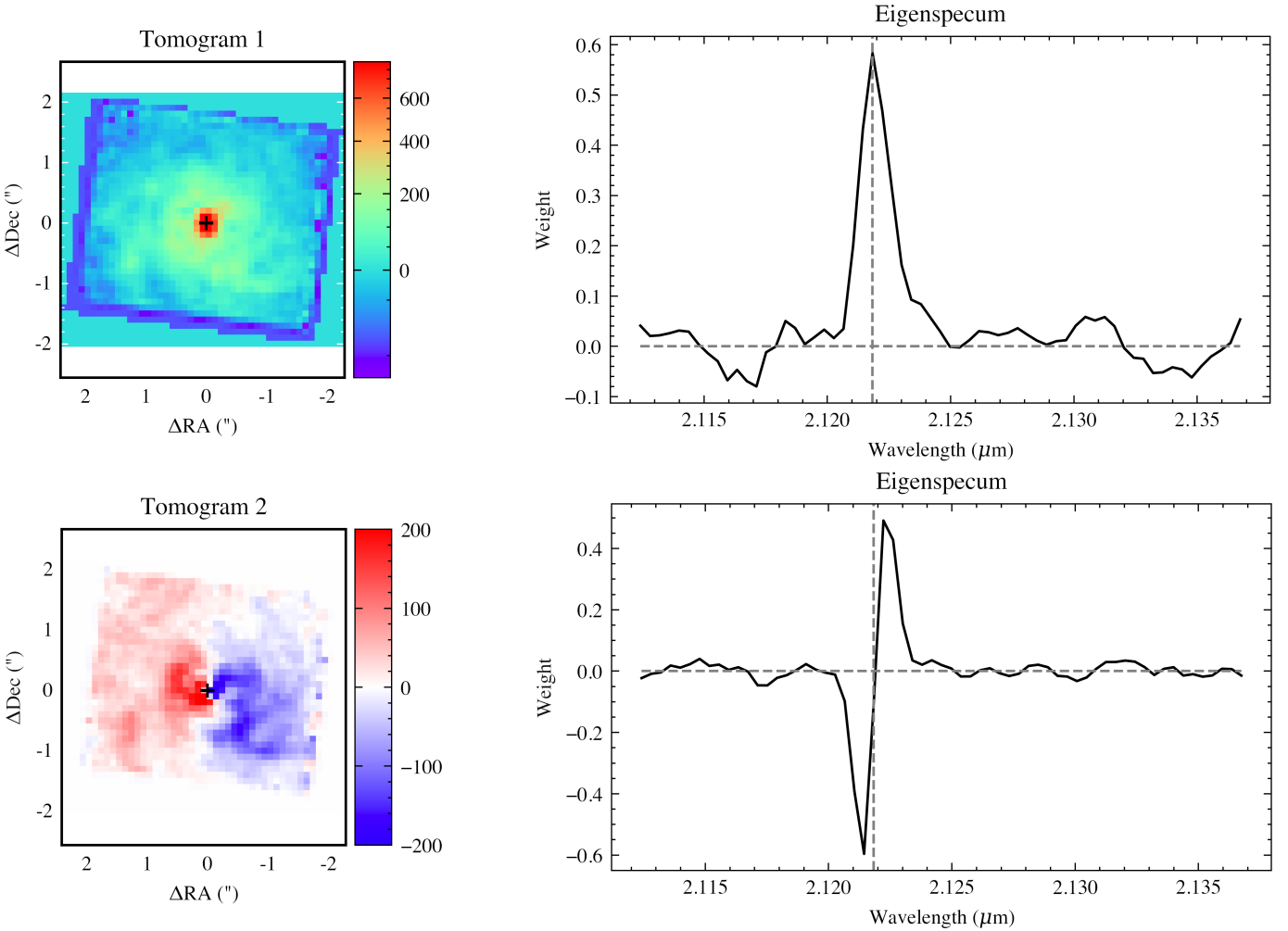


Figure 10. The first two principal components for a data cube of H_2 of NGC 3256 N. The left panels show the tomograms of each component which describes the spatial intensity of each eigenspectrum. The black crosses show the peak continuum position at this wavelength. The right panels show the eigenspectrum of each principal component. The horizontal dashed lines show where the weight is zero and the vertical dashed lines show the kinematic centre, determined by the peak wavelength of the first principal component. The first component describes the rest frame emission, while the second captures rotation of the gas.

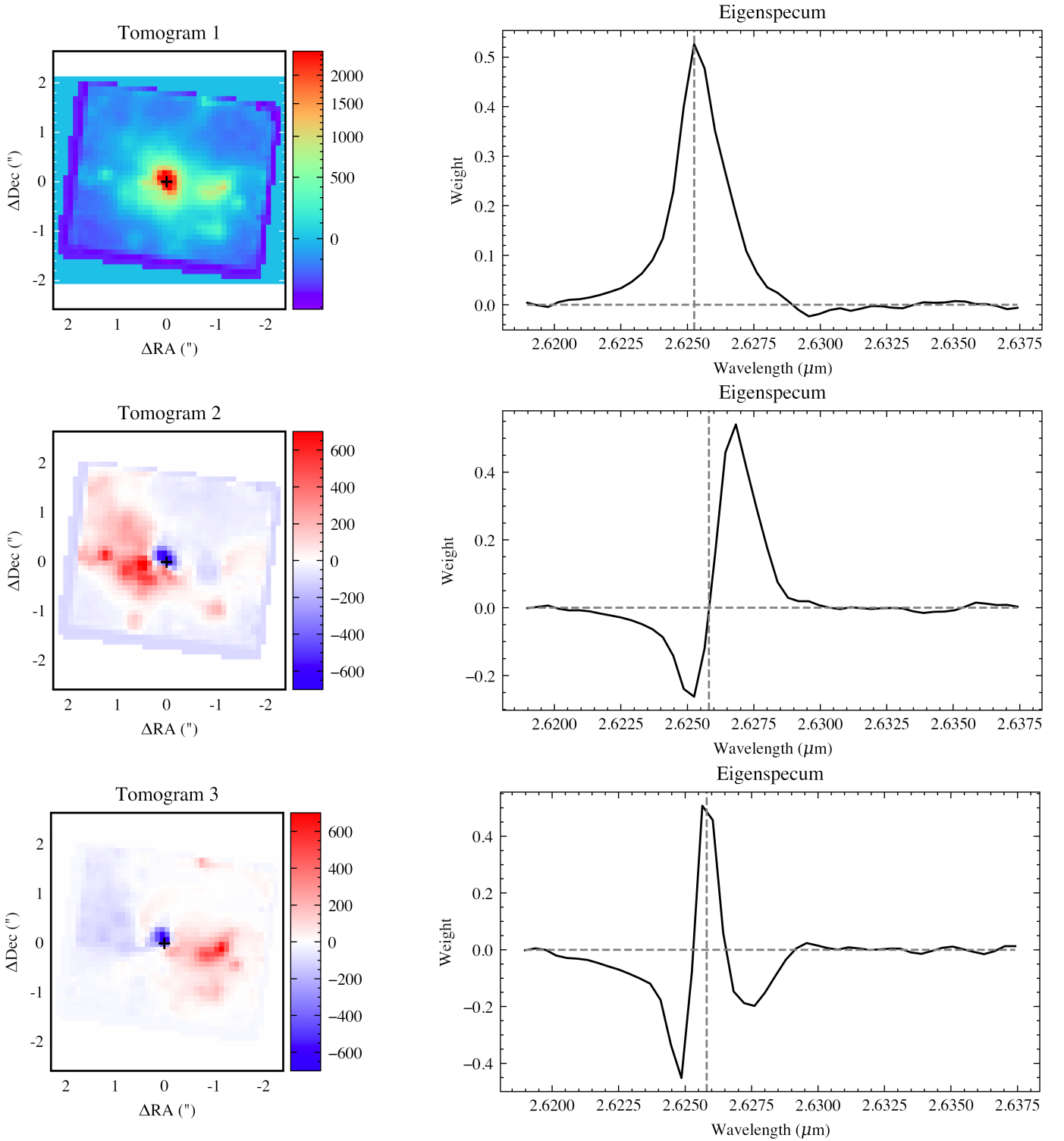


Figure 11. The first three principal components for a data cube of $\text{Br}\beta$ of NGC 3256 S. The left panels show the tomograms of each component which describes the spatial intensity of each eigenspectrum. The black crosses show the peak continuum position at this wavelength. The right panels show the eigenspectrum of each principal component. The horizontal dashed lines show where the weight is zero and the vertical dashed lines show the kinematic centre, determined by the peak wavelength of the first principal component. The first component describes the rest frame emission, while the second captures rotation of the gas and the third describes the velocity dispersion.

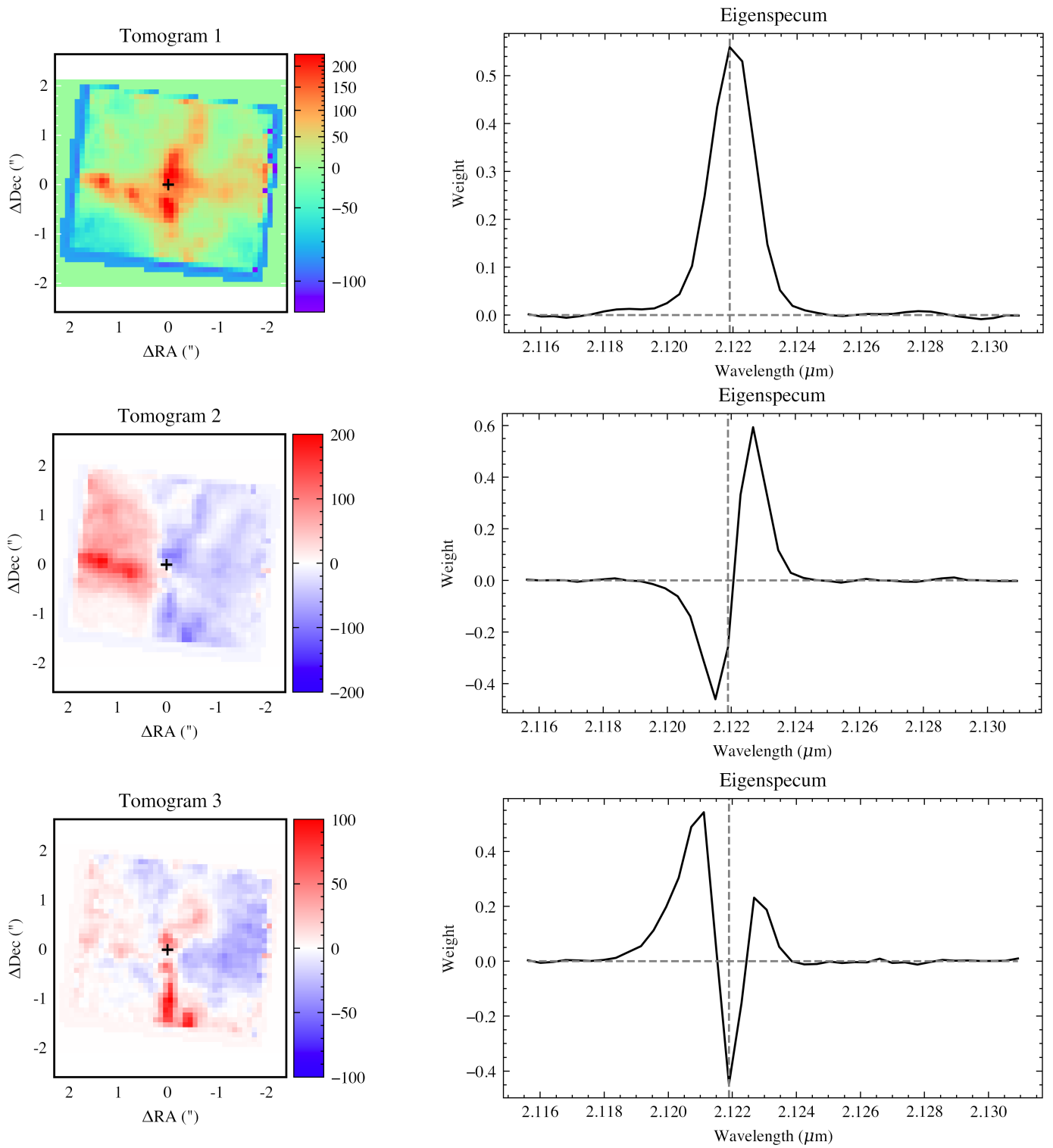


Figure 12. Same as Fig. 11 but for H₂ in NGC 3256 S.

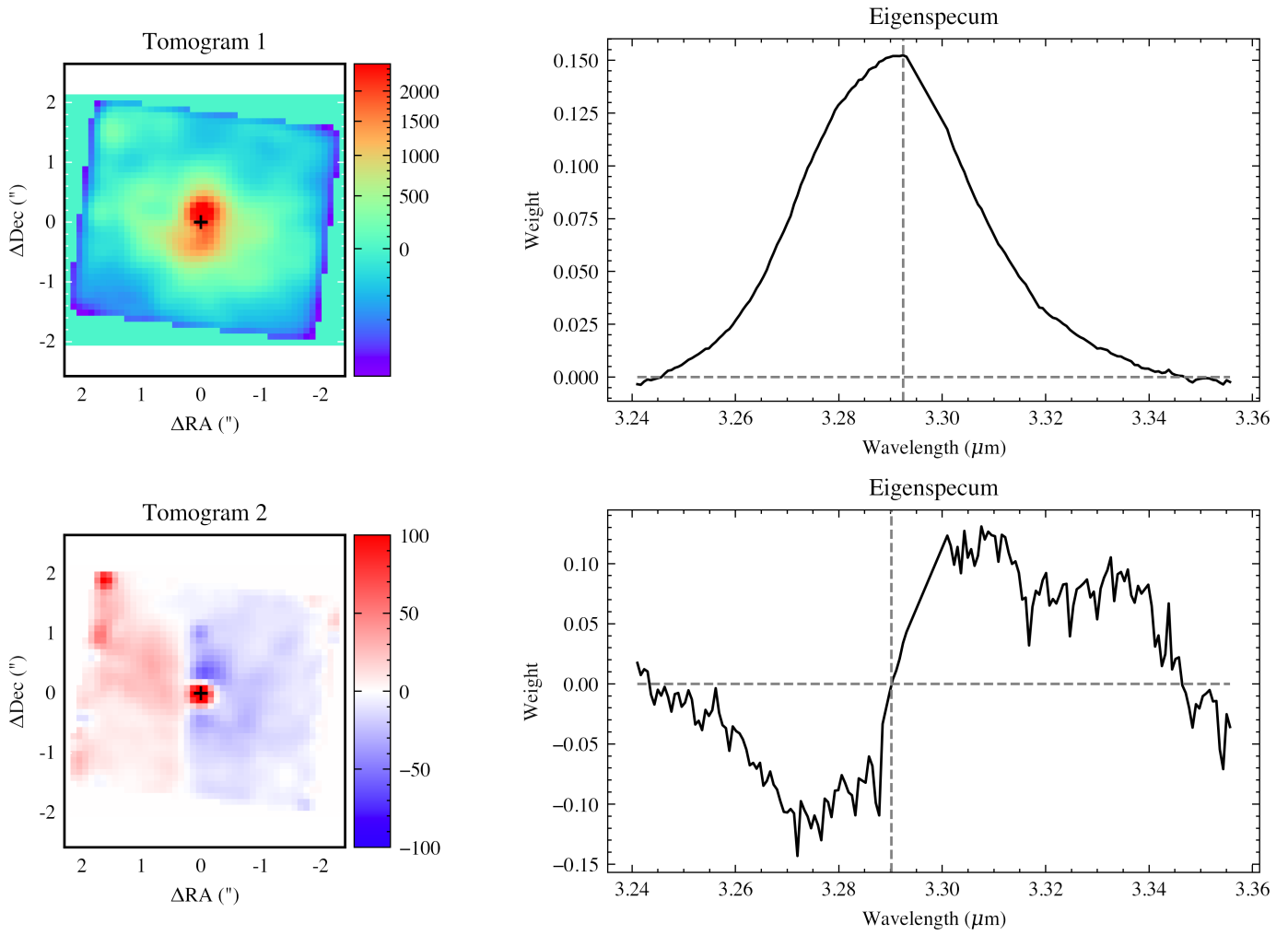


Figure 13. Same as Fig. 11 but for the 3.3 μm PAH in NGC 3256 S.

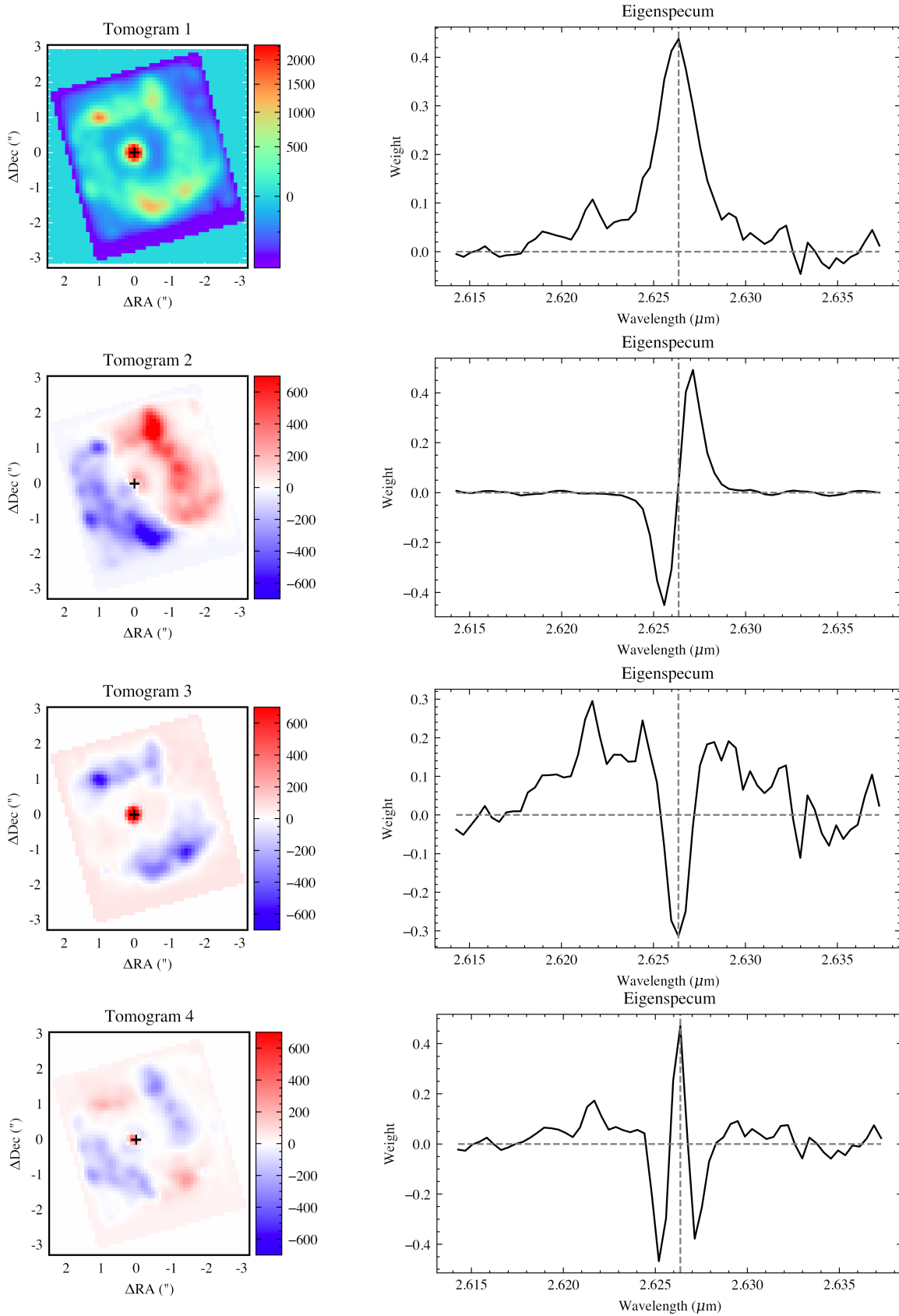


Figure 14. The first four principal components for a data cube of Br γ of NGC 7469. The first component describes the rest frame emission, while the second captures rotation of the gas. The third and fourth both show different components of the velocity dispersion, with the third isolating the broad line region of the AGN, with the very broad wings. The fourth component shows a higher velocity dispersion in the north-west and south-east of the star-forming ring, coinciding with the nuclear outflow.

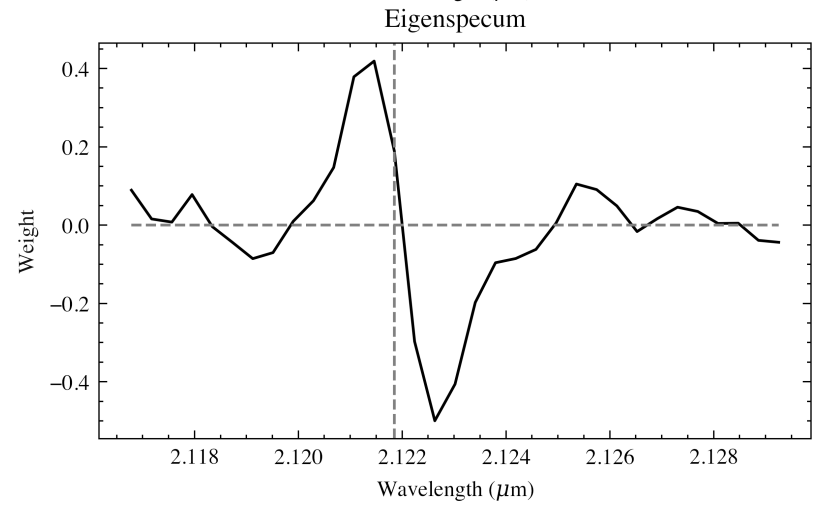
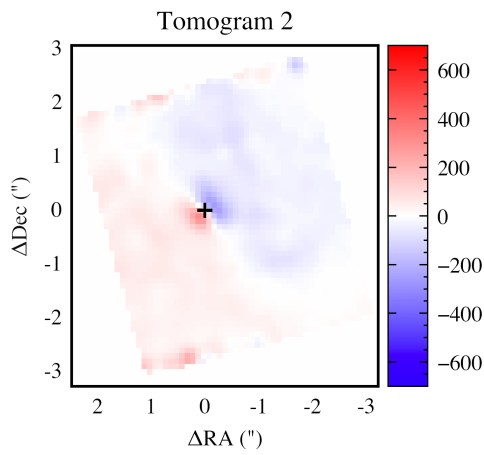
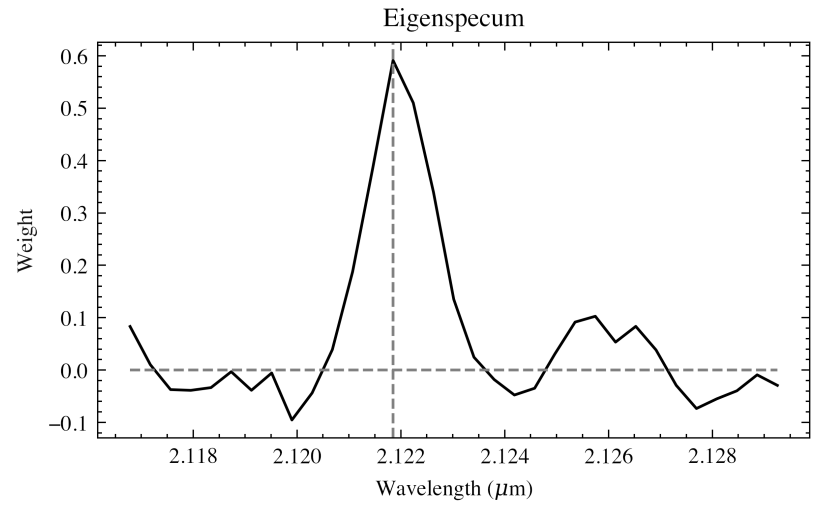
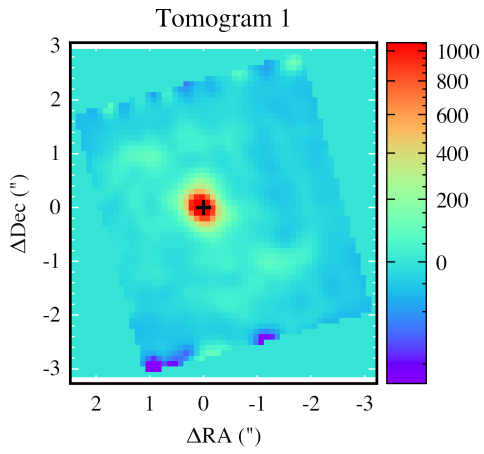


Figure 15. Same as Fig. 11 but for H₂ in NGC 7469.

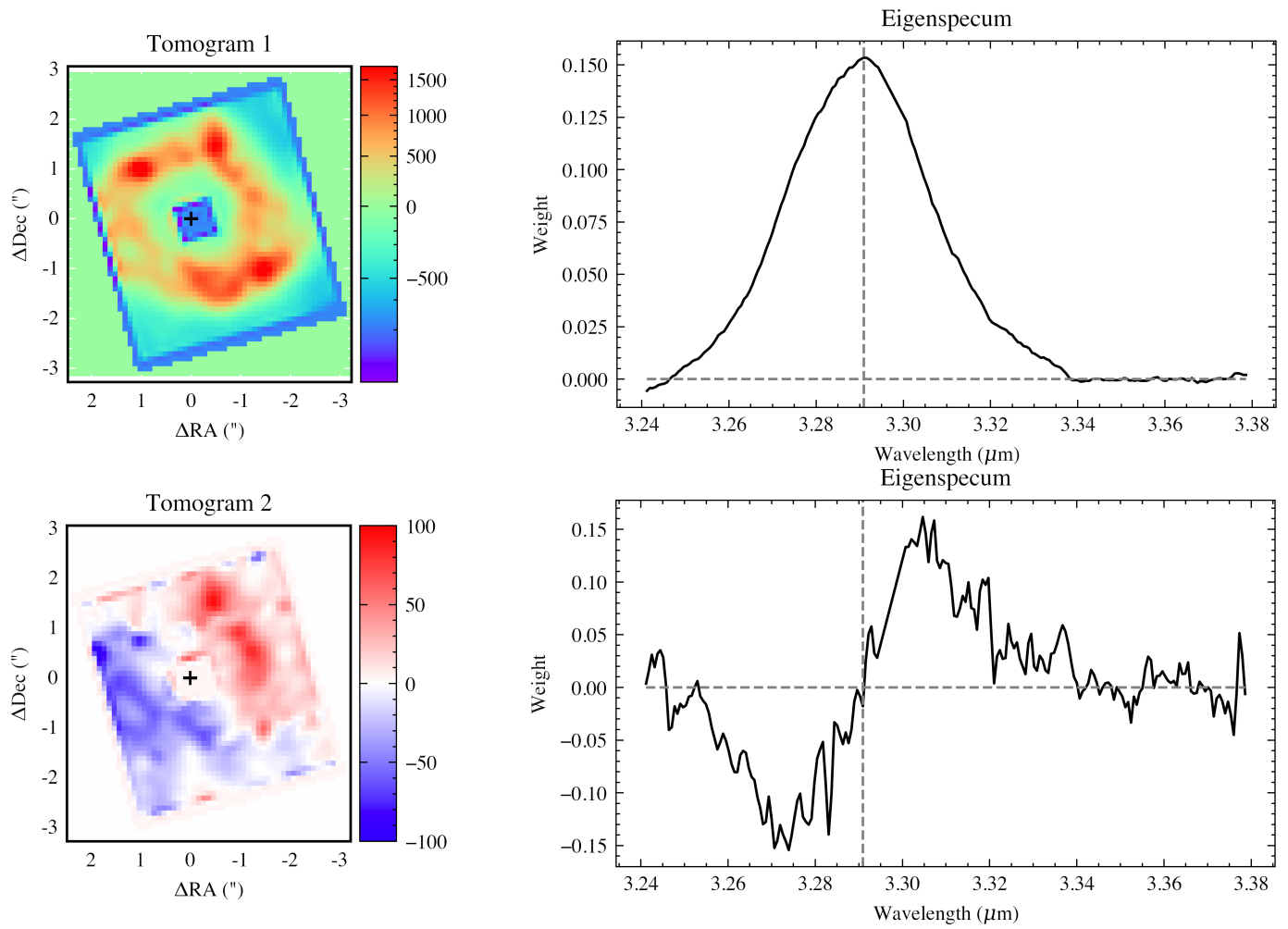


Figure 16. Same as Fig. 11 but for the 3.3 μm PAH in NGC 7469.